Available online at www.ijournalse.org

**Emerging Science Journal**

(ISSN: 2610-9182)

Vol. 10, No. 3, June, 2026

# Steady and Transient CFD Analysis of a Vertical Axis Ocean Current Turbine

Rasgianti [1*], Agus Suprianto [2], Ariyana D. Nugraha [1], Teguh Muttaqie [3], Ristiyanto Adiputra [3*]

[1] *Power Generation System Research Department, PT PLN (Persero) Research Institute, Jakarta Selatan 12760, Indonesia.*

[2] *Research Center for Aeronautics Technology, ORPA BRIN, Bogor 16350, Indonesia.*

[3] *Research Center for Hydrodynamics Technology, National Research and Innovation Agency (BRIN), Surabaya 60112, Indonesia.*

**Abstract**

Vertical-axis turbines (VATs) are a promising hydrokinetic technology for harvesting renewable energy from ocean currents. Still, their performance depends strongly on design parameters and flow interaction at different azimuthal angles. This study evaluates the performance of a VAT using computational fluid dynamics (CFD) simulations carried out under both steady-state and transient flow conditions. ANSYS CFX is used in the steady-state analysis to estimate torque and power output at various flow velocities and rotational speeds (RPM). At the same time, ANSYS Fluent is applied in the transient analysis to examine time-dependent torque behavior and azimuthal effects under unsteady flow. The steady-state results show that torque and power increase with higher flow velocity and rotational speed, reaching maximum values of 37,079 Nm and 291.86 kW at 4 m/s and 40 RPM. The transient results indicate periodic torque oscillations that become more stable at higher flow velocities, with peak turbine efficiency at 3 m/s, followed by a decrease at 4 m/s due to possible hydrodynamic losses. These findings provide clearer insight into VAT performance under realistic operating conditions and may support future efforts to improve hydrokinetic turbine design.

**Keywords:**

Ocean Current Energy;
Vertical Axis Turbine (VAT);
Computational Fluid Dynamics (CFD);
Transient Flow; Steady State.

**Article History:**

| | | | |
|---|---|---|---|
| **Received:** | 09 | November | 2025 |
| **Revised:** | 21 | April | 2026 |
| **Accepted:** | 03 | May | 2026 |
| **Published:** | 01 | June | 2026 |

## 1- Introduction

Converting the kinetic energy from seawater movement through ocean current turbines into mechanical energy to drive an electric generator is a promising approach for producing clean, sustainable electricity. According to Finkl & Charlier [1], the global potential power from ocean currents is estimated at approximately 450 GW, with a market value of around US$550 billion. Compared to wind, wave, and solar energy, ocean current power generation is relatively more predictable and stable [2]. Most ocean currents flow horizontally and are typically fastest near the surface with a dominant direction, although notable temporal variations can sometimes occur.

Vertical-axis turbines (VAT) are a promising technology for harnessing ocean current energy, as their rotor shafts are oriented perpendicular to the flow, allowing energy extraction from currents approaching from multiple directions without the need for an alignment mechanism. Several blade configurations have been developed, including the Darrieus type, which operates based on lift forces, and the Savonius type, which relies on drag forces generated by the flow [3]. In addition to their omnidirectional capability, VATs offer advantages in ease of maintenance and structural stability, particularly in deep-water or floating platform applications. Although their efficiency is generally lower than that of horizontal-axis turbines, advancements in blade geometry and structural optimization have shown potential to enhance performance and reduce torque fluctuations [4].

---

[*] **CONTACT**: rasgianti1@pln.co.id; ristiyanto.adiputra@brin.go.id

**DOI:** https://doi.org/10.28991/ESJ-2026-010-03-04

The development of vertical-axis turbines continues to encounter several technical challenges. Blade optimization remains a primary issue, as it significantly influences hydrodynamic performance and overall energy conversion efficiency [5]. Structural stability under fluctuating ocean current conditions is another critical concern, directly affecting turbine durability and operational safety. Furthermore, achieving high energy efficiency while preserving self-starting capability remains a persistent design limitation. Continued research and experimental validation are therefore essential to enhance the design, performance, and hydrokinetic characteristics of VATs. Such studies are crucial for advancing the development of efficient, reliable, and practical ocean current turbines for real-world applications.

In response to the need for enhanced performance and alternative design strategies, a previous study by Inácio et al. [6] conducted a numerical investigation of turbulent airflow in a hybrid Darrieus–Savonius vertical-axis wind turbine. Before analyzing the hybrid model, the study validated the numerical model by comparing simulation results for an isolated turbine with existing literature data. The numerical simulations were performed using the finite volume method in ANSYS Fluent, solving the time-averaged continuity and momentum equations with the k–ω SST turbulence model. The results demonstrated that the hybrid turbine achieved a substantial improvement in the power coefficient (Cp) at low tip speed ratios (TSR), increasing by approximately 70% at TSR = 0.75, indicating enhanced self-starting capability relative to a conventional Darrieus turbine. At the optimal TSR (1.5), the hybrid turbine continued to outperform the traditional Darrieus configuration by approximately 6.5%, suggesting that the addition of the Savonius rotor provides greater aerodynamic benefit than the induced flow disturbances. The study further quantified the aerodynamic contribution of each rotor component by comparing hybrid and isolated configurations.

Ghafoorian et al. [7] addressed the well-known self-starting problem of Darrieus-type VAWTs. by introducing a hybrid Darrieus–Savonius configuration aimed at improving performance at low tip speed ratios (TSR) by enhancing the power coefficient (Cp) and torque coefficient (Cm) at the initial azimuth angle. Unlike the common single-shaft hybrid design, which often exhibits reduced efficiency at high TSR due to the limitations of the Savonius rotor, this research proposed a dual-shaft concept with a drivetrain. This arrangement maintained the Savonius rotor at an optimal angular velocity of 19.79 rad/s. The numerical results demonstrated a 35% increase in Cp at low TSR and a 25% improvement at high TSR, indicating enhanced overall performance across a wide operating range.

Following earlier investigations into hybrid design solutions and rotor control, a subsequent study by Prasanna Vasan et al. [8] analyzed the aero-acoustic characteristics of an H-type VAWT with various cavity configurations using numerical simulation. The turbine geometry was modeled using SOLIDWORKS and simulated in ANSYS Fluent by solving the unsteady Navier–Stokes equations with the SST k–ω turbulence model. Levels of noise were predicted using the Ffowcs Williams–Hawkings (FW–H) analogy. The study evaluated five cavity configurations (TESC, TEDC, LESC, LEDC, and BASE) at two chord positions (0.25c and 0.75c). The TESC configuration demonstrated the highest power improvement, achieving a 72.5% increase relative to the BASE, while also exhibiting improved wake recovery and self-starting capability. From an acoustic perspective, TESC and TEDC configurations produced lower noise levels at low TSR, whereas the LESC and LEDC configurations were quieter at higher TSR. Overall, the findings indicate that cavity configuration significantly influences the aerodynamic performance and acoustic behavior of VAWT, highlighting their potential for use in urban applications.

Wong et al. [9] explored the effect of blade inertia on straight-bladed VAWTs using a 2-blade NACA0018 experimental model. The researcher applied two coating materials, epoxy and thin-film, to modified blade masses and inertia, and tested the blades in a wind tunnel at 5.61 m/s. The results showed that higher inertia led to longer acceleration times, greater transient fluctuations, and lower rotational speed and power output. In contrast, blades with lower inertia increased rotational speed by up to 30% and improved the maximum Cp by approximately 69.75%. These findings demonstrate that enhancing VAWT performance is not only dependent on blade geometry but also on the physical properties of the materials used.

Building on previous research into geometric modifications, self-starting solutions, and blade inertia, the next study by Shanab et al. [10] explored the use of flow augmenters (deflectors) on DR-SBVAWT turbines. Various deflector angles were tested using 2D transient CFD simulations. The β = 0° configuration exhibited the best performance, increasing TSR by 6% compared to β = 55° and by 11.5% compared to the no-deflector case, while improving efficiency by 30.15% at TSR = 2.5. These results demonstrate that external structural adaptations can effectively control incoming flow without changing the rotor design.

Further improvements were also studied using a trailing-edge device. Kord et al. [11] examined the effect of Gurney Flaps (GF) on a J-shaped Darrieus blade, with inboard, outboard, and double-sided placements at varying heights. Analysis of the power curve, vorticity, and pressure distributions indicated that an inboard GF with a height of 0.75% of the chord length yielded the best performance, enhancing efficiency by 12.35% at high TSR. In contrast, the outboard and double-sided configurations did not result in any performance improvements, indicating that flap placement is more critical to performance than flap size.

The latest study by Prabowoputra et al. [12] utilized 3D modeling of the Bánki turbine to analyze the effects of blade angle and the number of blades on the coefficient of power (Cp). The results indicated that a 40-blade runner with a 15 ° blade angle achieved the highest Cpmax, delivering the best performance across all blade configurations. Factorial design analysis confirmed that the blade angle has a greater influence on Cp than the number of blades, and there is an interaction between the two factors. The study concluded that the optimal design consists of a 15° blade angle and 40 blades, providing a foundation for further advancements in blade geometry to enhance the Bánki turbine's energy conversion efficiency.

Many studies, as highlighted in the literature review, have focused on improving the performance of ocean current turbines through blade geometry optimization, the integration of aerodynamic devices, and CFD-based numerical analysis. However, most of these studies have primarily addressed steady-state or average performance. In contrast, the unsteady flow characteristics and real-time torque behavior factors that significantly influence dynamic performance remain underexplored, particularly under variable ocean-current conditions. To address this gap, this study investigates the performance of a Vertical Axis Turbine (VAT) using both steady-state and transient CFD simulations. Unlike previous research, which relied on a single solver, this study uses ANSYS CFX for steady-state analysis and ANSYS Fluent for transient analysis. The turbine is tested at varying current speeds (2–4 m/s) and rotational speeds, revealing time-dependent interactions between torque, power, and efficiency. By capturing both steady and dynamic flow behaviors, the results show complex oscillatory patterns and nonlinear efficiency trends that are often overlooked in conventional steady-state studies. These findings provide valuable insights for optimizing turbine design and enhancing operational stability. A conceptual diagram illustrating the progression from previous research approaches to the proposed methodology of the present study is shown in Figure 1.

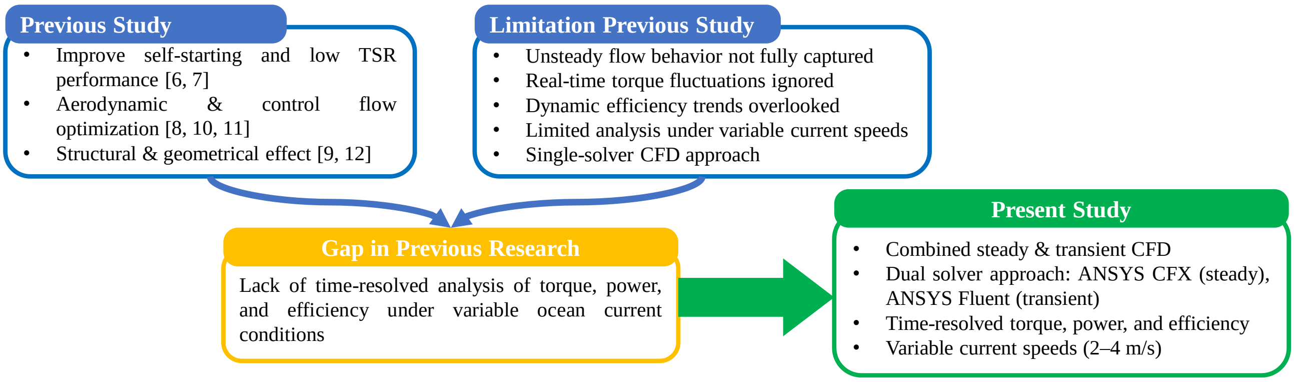

**Figure 1.** **Conceptual framework illustrating previous studies, identified research gaps, and the proposed approach of the present study**

## 2- Methods

Figure 2 illustrates the overall workflow adopted for conducting numerical simulations using Computational Fluid Dynamics (CFD) for ocean current turbine analysis in ANSYS CFX and Fluent 2024. The use of two solvers was determined by their suitability for different flow regimes, rather than by preference. Steady-state simulations were performed using ANSYS CFX, chosen for its robust convergence characteristics, which are enabled by a fully coupled pressure-velocity solver under quasi-steady flow conditions. Meanwhile, transient simulations were conducted in ANSYS Fluent, which offers advanced time-integration flexibility and sliding-mesh capabilities, making it well-suited for capturing unsteady hydrodynamic behavior and time-varying turbine torque. The workflow begins with simulation case preparation, including geometry modeling, mesh generation, and the assignment of appropriate boundary and initial conditions. This is followed by sequential execution of steady-state and transient analyses to capture both mean flow characteristics and time-dependent phenomena. The CFD model setup, including domain configuration and boundary conditions, was validated against benchmark data from previous literature to ensure the accuracy and reliability of the simulation results.

In the steady-state simulation, it is assumed that the flow variables do not change with time [13, 14]. Convergence in this analysis is crucial and is assessed by comparing the number of mesh elements with the torque acting on the turbine. The mesh resolution must be refined until the changes in these monitored parameters fall within acceptable limits. If convergence is not achieved, adjustments to the mesh, solver settings, or boundary conditions may be necessary. Once a stable solution is reached, the results proceed to the post-processing stage for performance evaluation and flow visualization.

For the transient analysis, which accounts for unsteady phenomena such as vortex shedding, dynamic loading, and wake behavior, the governing equations are solved at discrete time steps to capture the temporal variations in the flow field [15]. Similar to the steady-state process, convergence is monitored throughout the simulation to ensure solution accuracy. Although transient simulations require greater computational resources and time, they provide more detailed insight into the turbine's dynamic response, particularly the variation of torque and power over time.

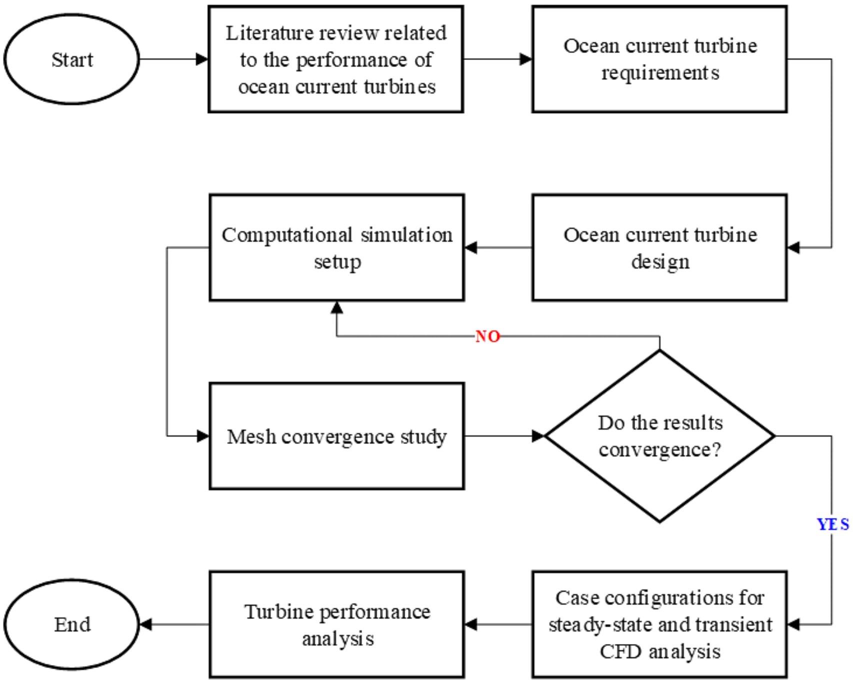

Figure 2. Flowchart of Methodology

The motivation for conducting transient CFD analysis was to gain a deeper understanding of the dynamic behavior of the designed turbine under realistic operating conditions. This includes time-dependent phenomena such as torque fluctuations, power output variations, and the turbine's ability to generate power during self-starting at very low flow velocities. By capturing unsteady effects such as vortex shedding, dynamic loading, and wake development, the transient analysis offers a more comprehensive evaluation of turbine performance, extending beyond the insights of steady-state simulations.

## 2-1- Steady-State Setup

### 2-1-1-Domain and Boundary Condition Settings

The computational domain for the 3D model of a Vertical Axis Turbine (VAT) with an H-Darrieus configuration, selected based on Rezaeiha et al. [16], has a diameter of 3.6 meters and a blade length of 5 meters. The domain size must be sufficiently large to accurately capture the fluid flow dynamics around the turbine while avoiding unwanted boundary effects. It is essential to consider factors such as flow direction, the distance to the domain walls, and adequate space for wake development [17]. The primary objective is to ensure that the turbine geometry does not affect the domain boundary conditions, thereby preventing the generation of unrealistic numerical results. The computational domain must be large enough to allow the fluid wake to develop freely and to prevent any unwanted interaction between the fluid flow and the domain walls. Detailed domain dimensions shown in Figure 3.

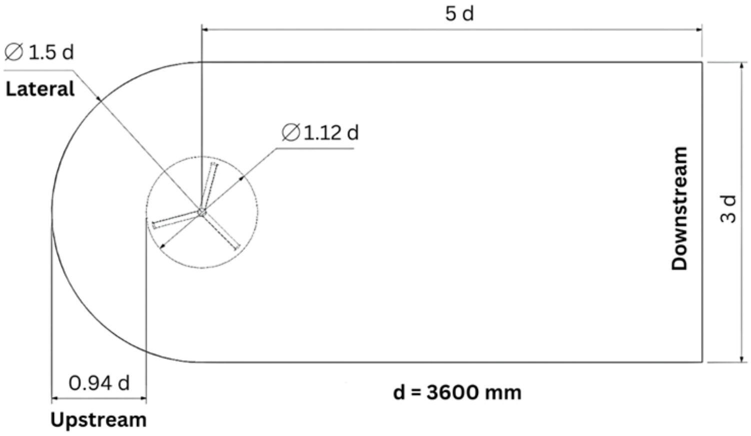

Figure 3. 3-D Single Turbine Domain Size Scheme for CFD Pre-Processing

In CFD simulations of a VAT, the computational domain is divided into a stationary region and a rotating (rotary) region to capture the fluid flow dynamics around the turbine accurately [18]. The rotary domain encompasses the rotating turbine components, while the stationary domain represents the non-moving surrounding fluid. Boundary conditions are applied to simulate realistic flow behavior: a velocity inlet at the upstream, a pressure outlet at the downstream, and symmetry or opening conditions at the far-field boundaries. An interface connects the two domains, with flow interaction managed using either the Sliding Mesh or MRF methods. The turbine is modelled in two configurations: a full system (three blades with supporting arms) and a blade-only configuration, to evaluate their effects on flow interaction and turbine performance (see Figure 4).

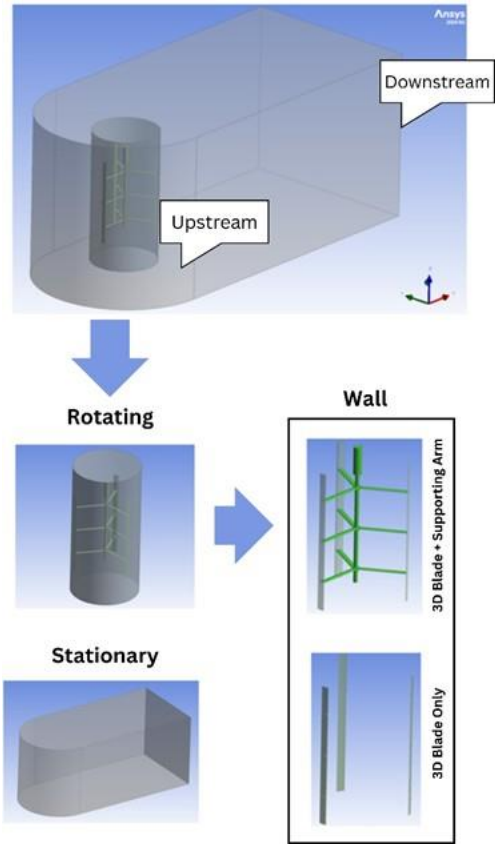

**Figure 4. Boundary Condition**

In the simulation, mesh control is applied using a Body of Influence (BOI), which allows local mesh refinement in specific areas of the computational domain that require higher resolution, such as around the turbine and in the wake region [19]. BOI is particularly useful in vertical axis turbine simulations to accurately capture wake development, including vortex shedding, blade–wake interactions, and significant variations in velocity and pressure distributions [20]. To enhance wake modeling, the researchers created an additional domain with a denser mesh focused on this region. In ANSYS CFX, this feature is called a Body of Influence (BOI), as illustrated in Figures 5 and 6, with the domain setup summarized in Table 1.

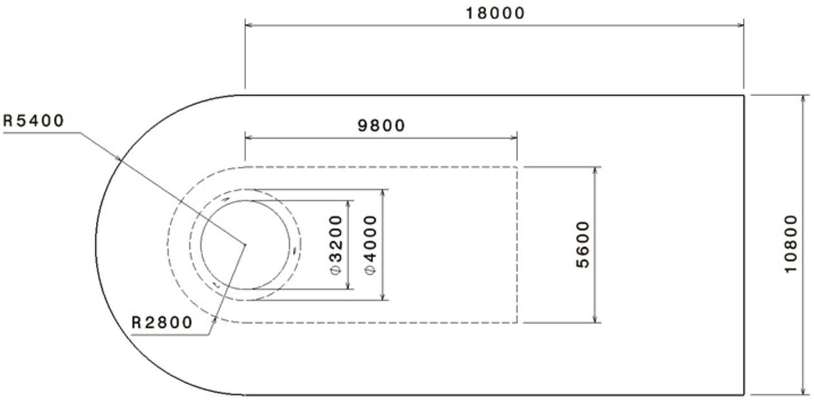

**Figure 5. Domain Size Scheme with Body of Influence (BOI) for CFD Pre-Processing**

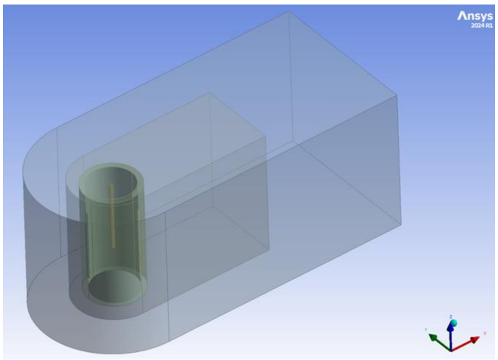

**Figure 6.** Domain With Body of Influence (BOI)

**Table 1.** Domain Setup

| Domain | Parameter | Detail |
|---|---|---|
| Stationary | Material type | Density: water, continuous fluid |
| | Reference Pressure | 0.690846 atm |
| | Buoyancy Model | Gravity Z-direction -9,8 m/s$^2$ |
| | Inlet Type | Velocity inlet, subsonic, cartesian velocity component (u: axial speed (m/s); v: 0 m/s; w: 0 m/s), turbulence (medium intensity 5%). |
| | Opening Farfield Type | Free wall |
| | Outlet Type | Pressure outlet, subsonic, average static pressure (relative pressure: 0 atm) over whole outlet |
| Interface | Interface Type | Outside domain rotating (conservative interface flux) |
| | Model Type | Fluid |
| | Fluid Model | General connection Frame change: Frozen Rotor; Pitchchange: 3600; Mesh connection: GGI |
| Rotary | Motion Type | Rotating with angular velocity (rpm), rotating Z-direction |
| | Mesh Deformation | No mesh deformation |
| | Turbine Type | 2-blade turbine with supporting arm: wall, no slip, smooth |
| | Interface Type | Inside domain rotating (conservative interface flux) |
| Opening | Type | Subsonic, mass and momentum opening pressure (relative pressure: 0 atm), flow direction: normal to boundary condition, turbulence: medium intensity (5%) |
| Wake | Body of influence (BOI) | - |

### 2-1-2- Mesh Settings

Mesh convergence is essential to ensure accuracy in CFD simulations [21]. To achieve this, the geometry was meshed by dividing it into smaller elements, and a mesh convergence study was conducted to determine the optimal element size [22]. A grid independence study confirmed that the results remain stable beyond a certain mesh size. For vertical-axis ocean current turbines, a fine mesh is required in critical regions, such as the blades, wake, and boundary layer, to accurately capture performance indicators like the power coefficient, force distribution, flow separation, and vortex interactions. This reduces errors and improves confidence in the design evaluation [23].

In CFD simulations of vertical-axis ocean current turbines, the k-ω SST turbulence model is widely used due to its ability to accurately predict flow separation, particularly around turbine blades at high angles of attack (AoA) [24]. This model is especially effective at handling boundary-layer behavior, making it suitable for capturing complex flow phenomena such as dynamic stalls. The SST model achieves this by combining the strengths of the k-ω model near walls, where accurate boundary-layer resolution is critical, with the k-ε model in the free-stream region. It solves two transport equations for turbulent kinetic energy (k) and specific dissipation rate (ω) (Equation 1 and Equation 2), enabling robust performance in simulations involving separation and transition [25].

$$\frac{\partial(\rho k)}{\partial t}+\frac{\partial(\rho u_i k)}{\partial x_i}=P_k-\rho\beta^{*}\omega k+\frac{\partial}{\partial x_i}\left[\left(\mu+\sigma_k\mu_t\right)\frac{\partial k}{\partial x_i}\right] \tag{1}$$

$$\frac{\partial(\rho\omega)}{\partial t}+\frac{\partial(\rho u_i\omega)}{\partial x_i}=\frac{\gamma}{\nu_t}P_k-\rho\beta\omega^2+\frac{\partial}{\partial x_i}\left[\left(\mu+\sigma_\omega\mu_t\right)\frac{\partial\omega}{\partial x_i}\right]+2(1-F_1) \tag{2}$$

where, $Pk$ is Turbulent kinetic energy production, $\omega$ is Specific dissipation rate, $\beta^*$ is Model constants, $\rho$ is Fluid density, $t$ is Time, $u_i$ is Velocity component, $\gamma$ is Model constant coefficients related to turbulence production, $\nu_t$ is Turbulent viscosity, $\beta$ is Specific dissipation rate coefficient, $\mu$ is Dynamic viscosity, $\sigma_\omega$ is Transport coefficient for $\omega$, $F_1$ is Blending function for the transition between the k-ω and k-ε models, $\sigma\omega^2$ is Coefficients for the transition adjustment part.

The grid selection process is carried out using the Unstructured Mesh method, with the Inflation Program Controlled option used to control detailed calculations, such as boundary-layer thickness and the number of layers within the boundary layer on each defined surface. This approach is applied to specific parts of the model, such as the three straight blades and the single turbine. The results of the Unstructured Mesh for both modeling configurations are shown in Figures 7 and 8.

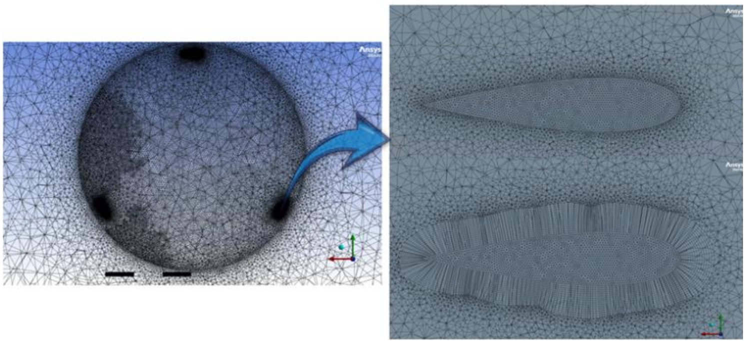

**Figure 7.** **3-D Model of Three Blades Only for Mesh Generation Processing**

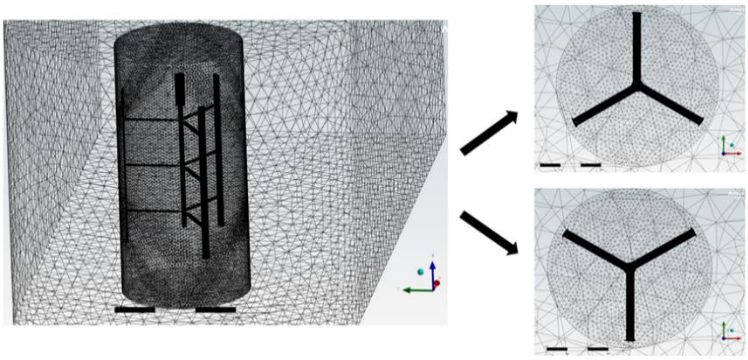

**Figure 8.** **3-D Model of Single Turbine for Mesh Generation Processing**

For each face, a face sizing is applied with a maximum range of $5x10^{-3}$ meters and a minimum of $1x10^{-4}$ meters for the single-turbine CFD simulation model. The mesh function is set to curvature, and the relevance center is assigned to the coarse, medium, and fine levels. Additionally, the first inflation layer thickness is set to approximately 0.05 meters, with a total of 11 layers. The mesh quality for the CFD simulation model with three blades, with or without a supporting arm, was 83% average element quality, 25.4% average skewness, and 77.3% average orthogonal quality. Statistically, the total number of elements ranges from 15,605,456 to 72,645,345, and the total number of nodes ranges from 3,489,522 to 10,856,394. The definition of the face properties for each boundary in each domain is provided in Table 2.

**Table 2.** **3-D Single Turbine Mesh Convergency Set-Up for CFD Pre-Processing**

| **Parameter** | **w/o Inflation (None Boundary Layer)** | | | |
|---|---|---|---|---|
| | **1** | **2** | **3** | **4** |
| Mesh Sizing | Coarse | Medium | Medium | Fine |
| Domain Mesh Size (m) | 0.7 | 0.5 | 0.3 | 0.3 |
| Domain Interface Mesh Size (m) | 0.1 | 0.04 | 0.03 | 0.03 |
| Domain Wall Mesh Size (m) | 0.005 | 0.003 | 0.003 | 0.0025 |
| Element Mesh | 10605720 | 28754924 | 31554923 | 41729194 |
| Node Mesh | 1989723 | 5422670 | 5962581 | 7882753 |

| **Parameter** | **With Inflation (11 Boundary Layer; 1st layer thickness 0.05 m)** | | | |
|---|---|---|---|---|
| | **1** | **2** | **3** | **4** |
| Mesh Sizing | Coarse | Medium | Medium | Fine |
| Domain Mesh Size (m) | 0.7 | 0.5 | 0.3 | 0.3 |
| Domain Interface Mesh Size (m) | 0.1 | 0.04 | 0.03 | 0.03 |
| Domain Wall Mesh Size (m) | 0.005 | 0.003 | 0.003 | 0.0025 |
| Element Mesh | 15605456 | 35254125 | 68574643 | 72645345 |
| Node Mesh | 3489522 | 8776678 | 9261523 | 10856394 |

The results of the mesh convergence analysis were plotted in graphs showing the torque generated by the turbine system as a function of mesh size (number of elements). Torque serves as the reference for evaluating the accuracy of the CFD simulation. A converged dataset indicates that once the mesh reaches a certain resolution, changes in torque values become minimal or insignificant (typically less than 1% to 2%) [26]. Numerical results show that although the torque displays distinct scalar values, it follows a similar trend across the graphs, reflecting high accuracy achieved with fine mesh sizes ranging from approximately 5 million to 70 million elements. As illustrated in Figure 9, the torque sensitivity stabilizes significantly at mesh sizes around 35 million elements. Therefore, the researchers selected an optimal mesh size of around 65 million elements for this vertical-axis turbine simulation to ensure high-accuracy results.

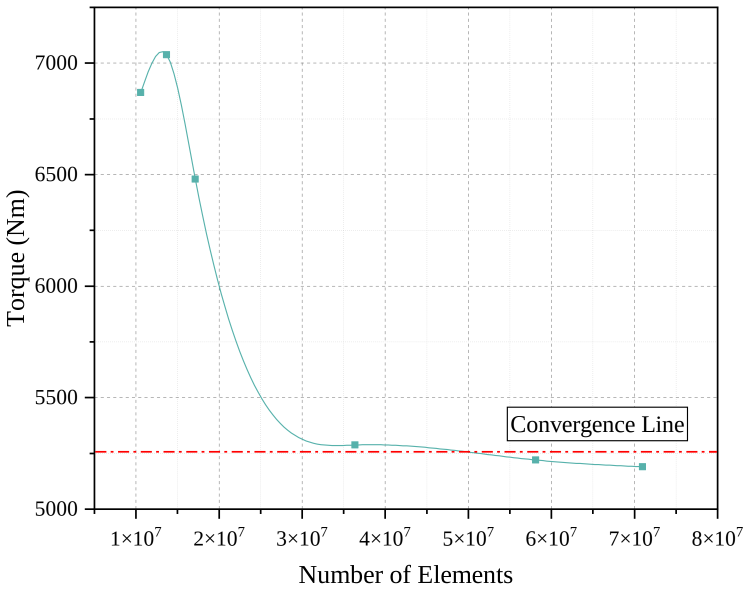

**Figure 9. Processing 3-D Mesh Convergency Analysis at 2 m/s and 40 rpm**

### 2-2- Transient Setup

The dynamic mesh model in computational fluid dynamics (CFD) is used to simulate systems where the geometry or mesh changes over time [27]. This approach is commonly applied in cases involving moving boundaries, such as piston motion in engines, flap deflection in aircraft, or turbine rotation in both vertical and horizontal-axis turbines. In dynamic mesh modeling, boundary motion can be classified as rigid (e.g., translation or rotation) or deformable (e.g., expansion or contraction), depending on the geometry involved.

Dynamic mesh simulations are computationally intensive due to frequent mesh updates and complex boundary conditions [28]. The time step size (Δt) is critical for achieving accurate, stable solutions. The Δt value should be small enough to capture the numerical solution of flow variables over time closely. For the transient simulations performed in this study, the primary variable is the ocean current velocity, tested at 0.7 m/s, 2 m/s, 3 m/s, and 4 m/s. By linking these input velocities to mesh size and applying a Courant number less than 1, the appropriate Δt value is calculated to ensure both numerical stability and solution accuracy.

$$Courant\ Number = \frac{characteristic\ flow\ velocity \times \Delta t}{typical\ cell\ size} = \frac{v \times \Delta t}{\Delta X} \tag{3}$$

The characteristics of ocean current velocity can be simulated using time step intervals (Δt), where each time step corresponds to one unit of simulation time [29]. The purpose is to monitor fluctuation in current velocity over time and determine the time required to reach the desired target speed. To model this behavior effectively, an exponential mathematical relationship between ocean current velocity and the time interval (Δt) is used, as expressed in Equation 4.

$$velocity\ magnitute = characteristic\ flow\ velocity * (u - exp\left(-\frac{\Delta t}{t}\right)) \tag{4}$$

One of the leading software packages used for transient simulations is ANSYS FLUENT 2024. Its dynamic mesh model enables the simulation of flows in which the domain geometry changes over time due to boundary motion, and it supports both single-phase and multiphase flows. The model applies generic transport equations to various physical models, including turbulence, energy, species, and phase.

Dynamic meshing in ANSYS FLUENT supports both steady-state and transient applications [30]. In transient simulations, the mesh is automatically updated at each time step based on the new boundary positions. Two motion types are available: prescribed motion, in which linear and angular velocities are defined as time functions relative to the object's center of gravity, and unprescribed motion, in which motion is computed dynamically based on force balance. The Six Degrees of Freedom (Six DOF) solver is commonly used for unprescribed motion, accounting for forces and moments acting on the solid body's inertia tensor.

In ANSYS FLUENT, translational and rotational motion relative to an object's center of gravity is calculated based on the forces and moments acting on it. This solver is specifically designed to model the motion of free-moving solid bodies in a fluid, capturing the interaction between the object and the fluid flow within its inertial coordinate system. The governing equation for translational motion used in the simulation is provided in Equation 5.

$$\overrightarrow{v_{gravity}} = \frac{1}{m}\sum \overrightarrow{F_{gravity}} \tag{5}$$

where, $\overrightarrow{v_{gravity}}$ is the velocity vector of the translational motion at the center of gravity (C.G) point, $m$ is Mass of rigid body, $\sum \overrightarrow{F_{gravity}}$ is the total force vector acting on the solid body mass relative to the center of gravity (C.G).

The governing equation for rotational motion, calculated based on the rigid body's coordinate point following Equation 6:

$$\overrightarrow{\omega_{body}} = L^{-1}\left(\sum \overrightarrow{M_{body}} - \overrightarrow{\omega_{body}} \times L.\overrightarrow{\omega_{body}}\right) \tag{6}$$

where, $L$ is Inertia tensor, $\overrightarrow{M_{body}}$ is the moment vector of the solid body (rigid body) relative to the center of gravity (C.G), $\overrightarrow{\omega_{body}}$ is the angular velocity vector of the solid body (rigid body).

Next, the moment of the solid body, $\overrightarrow{M_{body}}$, is the transformation of the inertia into the rigid body's coordinates, $\overrightarrow{M_{gravity}}$, with a multiplication factor of the constant transformation matrix R, as described in the following Equation 7:

$$\overrightarrow{M_{body}} = R\,.\overrightarrow{M_{gravity}} \tag{7}$$

with R is:

$$\begin{matrix} C_\theta C_\psi & C_\theta S_\psi & -S_\theta \\ S_\phi S_\theta C_\psi - C_\phi S_\psi & S_\phi S_\theta S_\psi + C_\phi C_\psi & S_\phi C_\theta \\ C_\phi S_\theta C_\psi + S_\phi S_\psi & C_\phi S_\theta S_\psi - S_\phi C_\psi & C_\phi C_\theta \end{matrix} \tag{8}$$

where the general function of the constants $C$ and $S$ is a function of $X$, where $X$ itself represents the angles $\phi$, $\theta$, and $\psi$, which are Euler angles corresponding to the rotation sequence around the z, y, and x axes.

$$C_X = Cos\ (X) \tag{9}$$

$$S_X = Sin\ (X) \tag{10}$$

To prepare a dynamic mesh model, several steps must be followed. First, the initial mesh convergence across the entire domain must be addressed, as explained in the previous section. Next, the motion in the moving zones should be defined, as also discussed in the previous section. Motion can be described using boundary profiles, User-Defined Functions (UDFs), or the Six Degrees of Freedom (Six DOF) solver. Fluent expects motion descriptions for face zones in 2-D models or cell zones in 3-D models. If the model includes both moving and stationary regions, these zones must be identified and grouped accordingly within the initial mesh.

Additionally, areas that deform due to motion from adjacent regions should also be grouped into separate zones. Non-conformal boundaries can be used to connect different zones through Fluent's non-conformal or sliding interface. For simulating 6 DOF motion, the specific requirements depend on the simulation objective. For a vertical-axis turbine blade simulation, only one degree of freedom (rotation around the z-axis) is required for the turbine's rigid body inertia. Input parameters such as the mass and moment of inertia of the turbine system (consisting of three blades and a supporting arm) need to be provided, as shown in Figure 10.

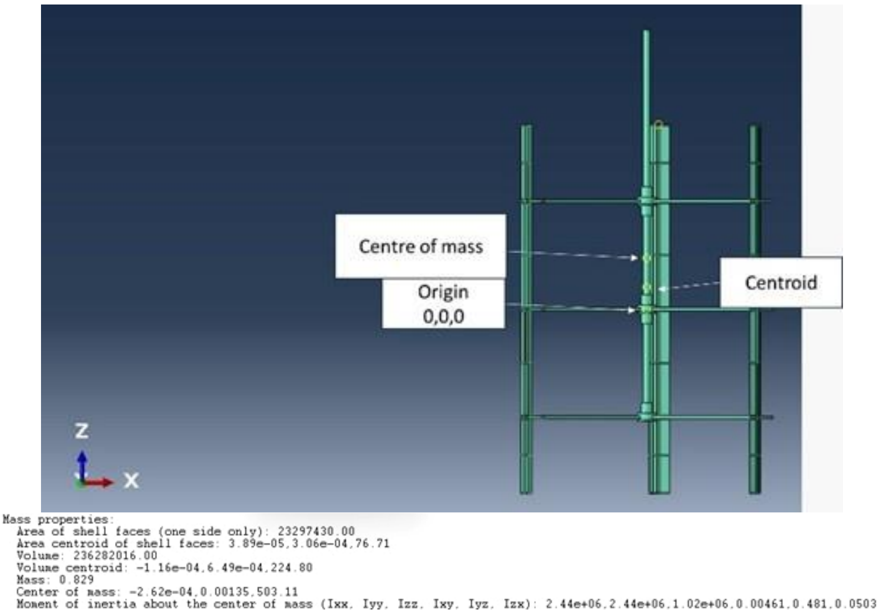

```
Mass properties:
  Area of shell faces (one side only): 23297430.00
  Area centroid of shell faces: 3.89e-05,3.06e-04,76.71
  Volume: 236282016.00
  Volume centroid: -1.16e-04,6.49e-04,224.80
  Mass: 0.829
  Center of mass: -2.62e-04,0.00135,503.11
  Moment of inertia about the center of mass (Ixx, Iyy, Izz, Ixy, Iyz, Izx): 2.44e+06,2.44e+06,1.02e+06,0.00461,0.481,0.0503
```

**Figure 10.** **Mass Properties of VAT**

## 3- Results

### *3-1- Steady-state Simulation*

#### *3-1-1- Single Vertical Axis Turbine with v = 2 m/s*

The performance of the three-blade vertical axis turbine is evaluated by analyzing the torque distribution (Nm) and power output (kW) against the azimuth position (°) for one full rotation cycle, using an axial current speed of approximately 2 m/s. The azimuth position is defined as the blade angle relative to the rotation axis, measured from 0° to 360°, allowing continuous identification of torque and power changes on each blade due to variations in angle of attack, wake interaction, and flow separation. In this test, the turbine shaft is operated at variable rotational speeds between 20 and 40 rpm to assess dynamic performance under different operating conditions. This includes observations of positive and negative torque, rotational stability, instantaneous power efficiency, and potential blade stall. This approach provides a detailed mapping of torque and power fluctuations across a full cycle, offering a deeper understanding of aerodynamic behavior and supporting potential improvements in blade design and speed-control strategies.

##### *3-1-1-1- Turbine Torsion vs. Azimuth Position*

Figures 11 and 12 present the flow vector and velocity contour results, showing how water moves between and around the turbine blades, which is crucial for understanding fluid–blade interactions. These flow patterns help identify acceleration zones, boundary-layer behavior, possible flow separation, and vortex formation. In ocean current turbines, vortices typically form at the trailing edge of the blades due to pressure differences, which can reduce efficiency and affect torque. The velocity contours show a flow range of 0–12.45 m/s, exceeding the inlet speed of 2 m/s due to blade rotation at 40 rpm, especially near the leading edge, where the flow is faster. At the blade tip, the velocity changes significantly from 3.11 to 9.33 m/s, potentially producing tip vortices and partial flow separation. Downstream of the turbine, a wake region forms, with velocities below 3 m/s and higher turbulence levels, indicating energy loss and unsteady flow conditions. These results help explain torque fluctuations and suggest that further improvements can be achieved through blade-shape optimization, pitch control, or additional flow-control devices, as described by Xiao et al. [31], to reduce flow separation and enhance turbine efficiency.

The pressure distribution on the turbine blade surface, shown in Figure 12, exhibits significant variations due to the interaction between water flow and the blade surface. In ocean current turbines, the leading and trailing edges are particularly critical, as noted by Arini et al. [32], because the flow speed changes rapidly, creating zones of high (positive) and low (negative or suction) pressure. CFD results indicate that the pressure around the blades ranges from –157,900 Pa to +565,500 Pa, indicating that some parts of the blade experience strong suction. In contrast, other areas experience high pushing forces. Higher pressure is observed along the blade edges, ranging from +2,934 Pa to +43,140 Pa, and around the turbine support arm, where the pressure is approximately +29,740 Pa. These pressures can increase structural load and stress. In contrast, the dynamic pressure around the blade is lower, between –144,500 Pa and –117,700 Pa, and around –77,490 Pa in the wake area, where the flow slows and becomes more turbulent. These positive and negative pressure zones are critical for generating lift and drag forces, which, in turn, affect torque and power performance. Pressure behavior is also influenced by factors such as fluid density, viscosity, depth effects, and hydrostatic forces, making it essential to consider these aspects in blade design, material strength assessment, and turbine control.

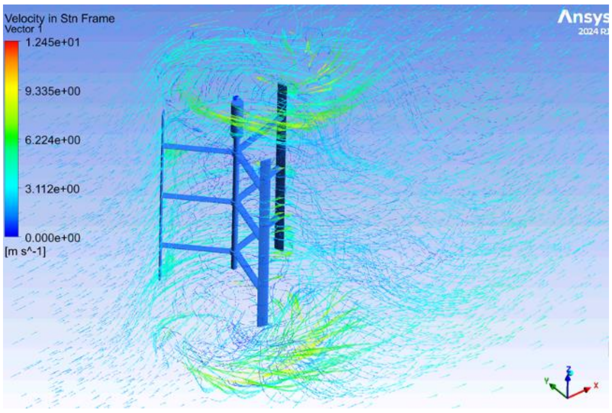

**Figure 11.** **Velocity in Stationary Frame: Vector and Scalar at v = 2 m/s and ω = 40 rpm**

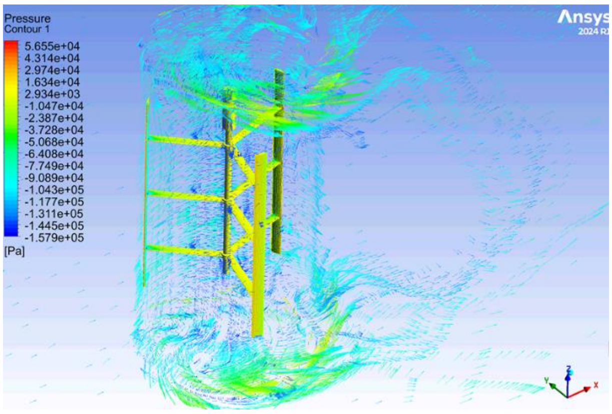

**Figure 12.** **Pressure Contour at v=2 m/s and ω = 40 rpm**

Figure 13 shows that the torque variation with azimuth position is not symmetrical, indicating uneven flow around the turbine throughout a complete rotation. This condition may be caused by non-uniform velocity distribution, changes in the incoming flow angle, and wake interaction among blades at different azimuth positions. Torque peaks occur at azimuth angles of 65°, 165°, and 270°, where the blades are at a more effective angle of attack, producing higher lift and maximum torque on the turbine shaft. In contrast, torque drops at azimuth angles of 110° and 240°, showing less efficient blade positions due to too small or too large angles of attack, as also found by Ayachi Amar et al. [33]. This reduces lift, increases drag, and can induce flow separation or stall. These results show that the aerodynamic performance of VAWT blades strongly depends on their rotational phase, emphasizing the need for optimized blade geometry and adaptive rotational speed control to mitigate negative torque and enhance power stability during each rotation.

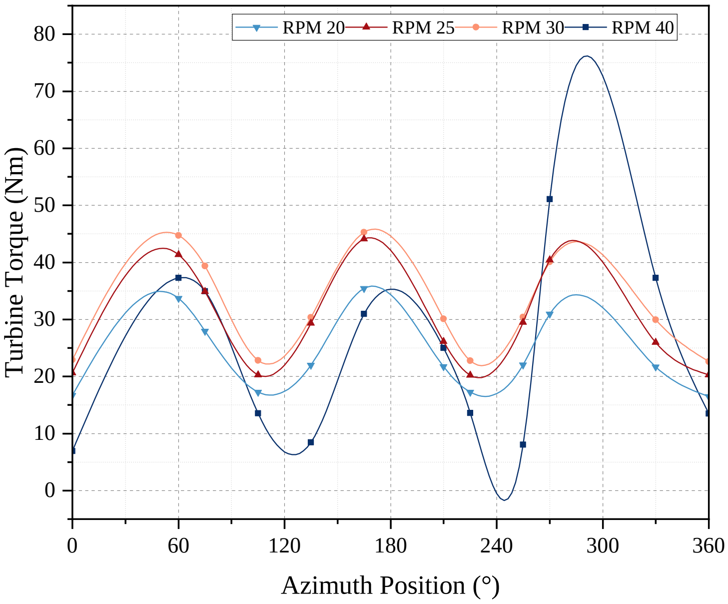

**Figure 13.** **Turbine Torque at v = 2 m/s with different RPM**

At lower rotational speeds between 20 and 25 rpm, the turbine generates its highest average torque of about 16,923 N·m, indicating that the blades operate at a more effective angle of attack and can capture a greater portion of the incoming flow's kinetic energy. However, as the rotational speed increases by increments of 5–10 rpm, the torque gradually decreases by approximately 14.49%-38.24%, reaching around 8,897 N·m at 40 rpm. This reduction occurs because the relative velocity difference between the water and blade surface decreases, leading to diminished lift and increased drag. These variations also reflect non-uniform hydrodynamic loading along the blades, resulting from wake interactions, fluctuating flow angles, and transitions between attached and partially separated flow regions. If torque fluctuations become too large, they may create negative dynamic effects such as increased vibration, reduced rotational stability, and fatigue loading on structural components, which could accelerate mechanical wear and lower the long-term energy efficiency of the turbine system.

### *3-1-1-2- Turbine Power vs. Azimuth Position*

In general, the electrical power produced by a vertical-axis turbine is directly governed by the torque generated by the blades and the turbine's rotational speed, where higher torque at an appropriate rotational speed results in greater power output. Figure 14 illustrates this relationship by presenting the distribution of power over one full rotation cycle, with several peaks and valley points that closely correspond to torque variations at specific azimuth angles. The turbine achieves its highest average power, ranging from approximately 44.103 to 45.26 kW, at moderate rotational speeds of 25-30 rpm, indicating that these speeds provide an optimal balance between lift production, drag reduction, and hydrodynamic efficiency. In contrast, the lowest power output occurs at 20 rpm and 40 rpm, with recorded values of 35.44 kW and 37.27 kW, showing that rotational speeds that are too low or too high reduce the energy capture efficiency, as also reported by Fernández-Jiménez et al. [34]. This is caused by insufficient angular momentum or a reduced relative velocity between the flow and the blade surface. The power curve also shows an asymmetric distribution, where peak values are not evenly spaced, especially between azimuth angles 260° and 360°, where the turbine operating at 40 rpm produces a local peak of about 52.12 kW. This uneven pattern is likely due to non-uniform flow around the rotor, including wake interaction, variations in the fluid approach angle, rotational flow effects, and local acceleration or deceleration zones that change the angle of attack and lift-to-drag ratio of each blade segment.

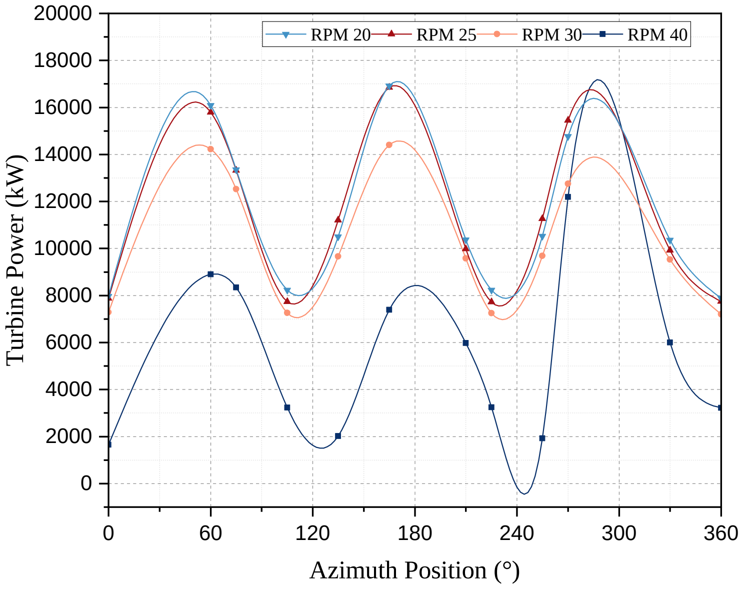

**Figure 14. Turbine Power at v=2 m/s with Different rpm**

As the turbine's rotational speed increases, more input energy is required, resulting in a reduction in torque. To maintain system stability, the turbine's power output rises correspondingly with increasing rpm. The power increases by about 24.5% from 20 to 25 rpm, but only by 2.62% between 25 and 30 rpm. At higher rotational speeds, the effective kinetic energy transfer weakens, making the turbine more susceptible to flow separation along the blades. Power recovery is observed between azimuth positions 250° and 270°, showing a significant 39.84% increase at 40 rpm. However, beyond 270° and approaching a full rotation (360°), the power output declines as the turbine's energy conversion diminishes.

### *3-1-2- Single Vertical Axis Turbine with v = 0.7, 1, 3, and 4 m/s*

Since the performance trends observed at low (0.7 and 1.0 m/s) and high (3.0 and 4.0 m/s) ocean current speeds exhibit torque–power behavior highly consistent with that at 2.0 m/s, only the maximum torque and power values are reported for these additional flow cases. This simplification is intended to maintain clarity and avoid unnecessary repetition, as the complete performance curves at different flow velocities exhibit similar shapes and peak patterns. Across all flow conditions, the highest torque and power outputs consistently occur within comparable azimuth angles and rotational speed ranges, with the primary differences appearing only in magnitude due to variations in dynamic pressure, flow momentum, and the strength of hydrodynamic blade–fluid interactions. Thus, emphasizing only the maximum values provides a focused understanding of peak operational capabilities without compromising the accuracy of performance interpretation.

As illustrated in Figures 15 and 16, at relatively low incoming current velocities (0.7–1.0 m/s), both torque and power increase steadily with increasing rotational speed from 20 to 40 rpm. This behavior indicates that the turbine operates within a stable aerodynamic region where the angle of attack remains effective, flow separation is minimal, and the hydrodynamic lift component dominates. However, at higher flow velocities between 3.0 and 4.0 m/s, the available kinetic energy increases significantly, leading to greater hydrodynamic loading, higher fluid-induced stresses, and a higher risk of partial or full-flow stall on the blades if the rotational speed is not sufficiently high. Under these conditions, rotational speeds greater than 40 rpm are likely necessary to maintain favorable flow attachment, avoid excessive negative torque zones, and preserve aerodynamic efficiency. These findings confirm that the optimal operating rpm is not fixed but varies according to current velocity, blade loading characteristics, and overall hydrodynamic balance, highlighting the importance of adaptive rotational control strategies, such as passive or active pitch regulation, flow-guiding devices, or real-time speed adjustment for improved performance and reliability across different ocean environments.

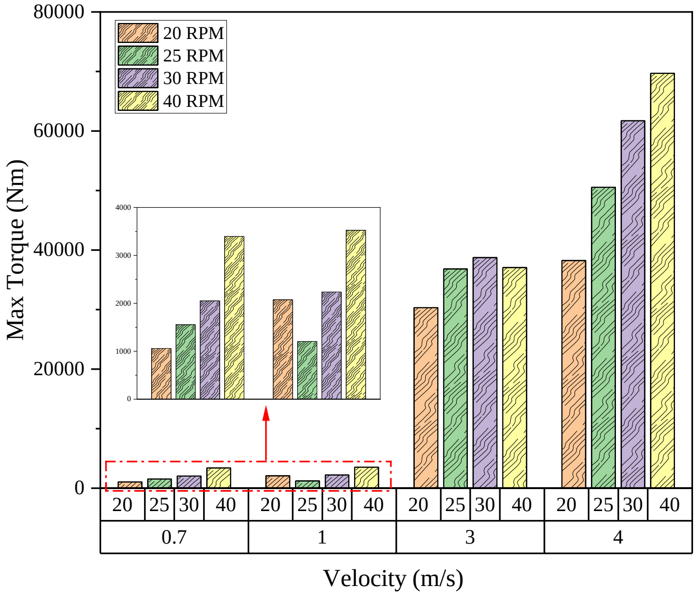

**Figure 15.** Max Torque for Each Variation

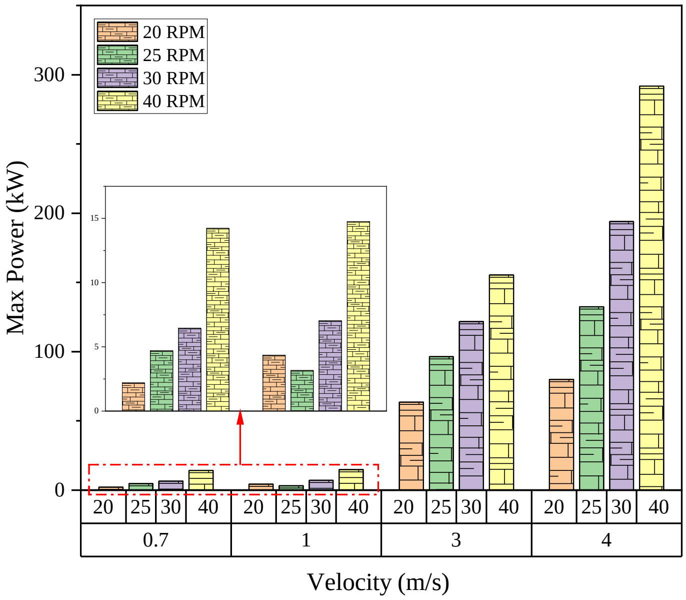

**Figure 16.** Max Power for Each Variation

### 3-2- Transient Simulation

### 3-2-1- Torque vs. Flow Time

The graph below illustrates the relationship between turbine torque and time stability, characterizing the turbine's power response to varying ocean current speeds. Initial observations, compared with Arini et al. [32], reveal an initial growth phase driven by the induced velocity of the incoming ocean current, followed by oscillatory behavior with decreasing amplitude, occasional outliers during the damped oscillation phase, and a final transition to a quasi-stable state. At a current speed of 0.7 m/s, the analysis presented in Figure 17 identifies two distinct phases. During the initial transient phase (approximately 0–5 seconds), a sharp torque spike is observed, reaching a peak value of around 1500 N·m before beginning to oscillate. This phenomenon is likely due to changes in initial conditions to aerodynamic transient effects. In the stable oscillation phase (from around 6 seconds onward), the graph displays a periodic oscillation pattern with a more stable amplitude, indicating that the system has reached a quasi-steady state. At this induction velocity, the turbine exhibits a free harmonic rotation with an angular velocity of approximately 3.3 rad/s. This behavior is strongly influenced by dominant factors such as the turbine's inertia model.

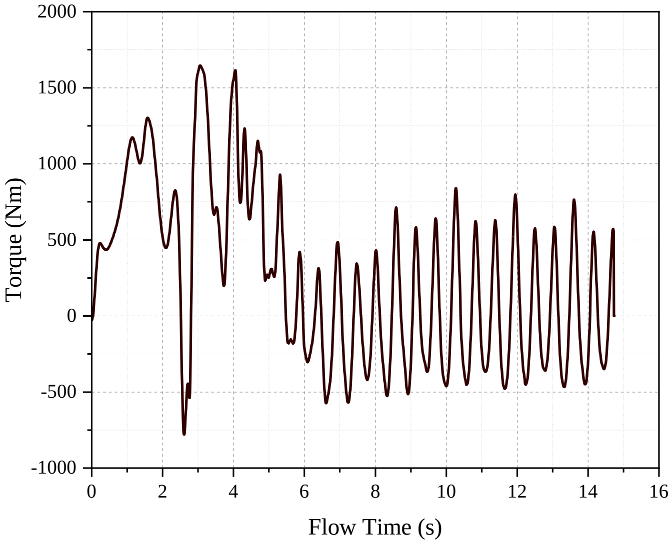

**Figure 17.** **Torque vs. Flow Time at a Flow Velocity of 0.7 m/s**

At a current speed of 2 m/s, the transient analysis presented in Figure 18 clearly demonstrates two distinct dynamic response phases associated with fluid–structure interaction and turbine rotational stabilization. During the initial transient period (approximately 0–2 seconds), the system exhibits large, irregular, and highly unstable oscillations, indicating that the turbine is still adapting to the sudden fluid loading and has not yet reached dynamic equilibrium. These fluctuations are likely caused by rapid variations in hydrodynamic torque, pressure imbalances around the blades, and momentary variations in rotational acceleration. Following the initial phase, the response transitions into a stable oscillatory regime (from roughly 2 seconds onward), where the oscillation amplitude becomes relatively consistent and periodic, reflecting that the flow field, vortex formation, and blade–fluid interaction have stabilized, allowing the turbine to operate under near–steady-state conditions. When compared with the oscillatory behavior recorded at a lower fluid velocity of 0.7 m/s, the oscillations at 2 m/s are noticeably faster, more energetic, and exhibit a higher amplitude, confirming that increased flow velocity results in higher dynamic pressure and greater hydrodynamic loading on the blades, which can enhance turbine torque and power generation potential, but may also introduce stronger unsteady forces that could influence long-term fatigue, vibration response, and structural integrity if not appropriately controlled or damped.

Similarly, the analysis at a current speed of 3 m/s, as presented in Figure 19, demonstrates a distinct two-phase dynamic response consistent with the trend observed at lower flow velocities. During the initial transient phase (approximately 0–2 seconds), the torque response displays large, irregular, and rapidly varying fluctuations, indicating that the turbine rotor and surrounding fluid field are still undergoing dynamic adaptation before reaching equilibrium. These fluctuations are attributed to sudden variations in flow momentum, unstable vortex formation near the blade surfaces, and non-uniform pressure distribution along the blade span as the turbine accelerates. After roughly 2 seconds, the torque waveform transitions to a stable oscillatory phase, in which the oscillations become more periodic and uniform in amplitude, suggesting that the hydrodynamic forces, blade–fluid interactions, and angular acceleration have stabilized under a quasi-steady operating condition. Additionally, the oscillation frequency at this flow speed is noticeably higher than at lower velocities (0.7, 1.0, and 2.0 m/s), which is most likely associated with the increased angular velocity of the turbine at 3 m/s, resulting in faster blade passing cycles and more frequent formation and shedding of vortices around the blade surfaces. This condition indicates that higher current velocities not only enhance the hydrodynamic loading and torque magnitude but also induce faster dynamic responses, which may improve power generation potential while simultaneously increasing the risk of structural fatigue, vibration, and long-term mechanical wear if not properly mitigated.

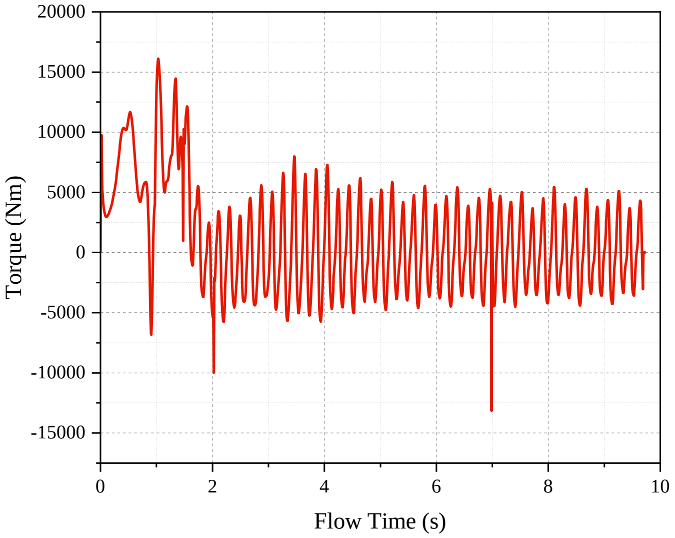

**Figure 18.** **Torque vs. Flow Time at a Flow Velocity of 2 m/s**

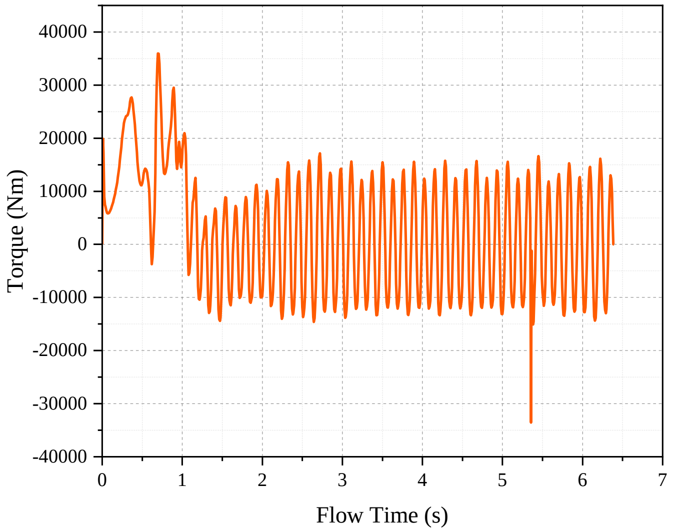

**Figure 19.** **Torque vs. Flow Time at a Flow Velocity of 3 m/s**

Figure 20 presents the time-based torque response of the turbine operating at a flow velocity of 4 m/s, with two primary phases of dynamic behavior clearly identified. During the initial transient phase, approximately between 0 and 1.5 seconds, the torque signal exhibits large, irregular, and rapidly varying fluctuations, indicating that the turbine is still adapting to sudden hydrodynamic loading, unsteady wake development, and spatial pressure gradients as the blades accelerate from rest. In this stage, the torque reaches a peak of about $6.5\times10^4$ N·m before gradually decreasing due to hydrodynamic damping and flow stabilization. After approximately 2 seconds, the response transitions into a stable oscillatory regime characterized by periodic torque variations of nearly uniform amplitude, signifying that the turbine has reached a quasi–steady-state aerodynamic and hydrodynamic operating condition. The remaining oscillations are attributed to continuous variations in angle of attack, periodic vortex shedding, and blade-fluid interaction during each rotational cycle.

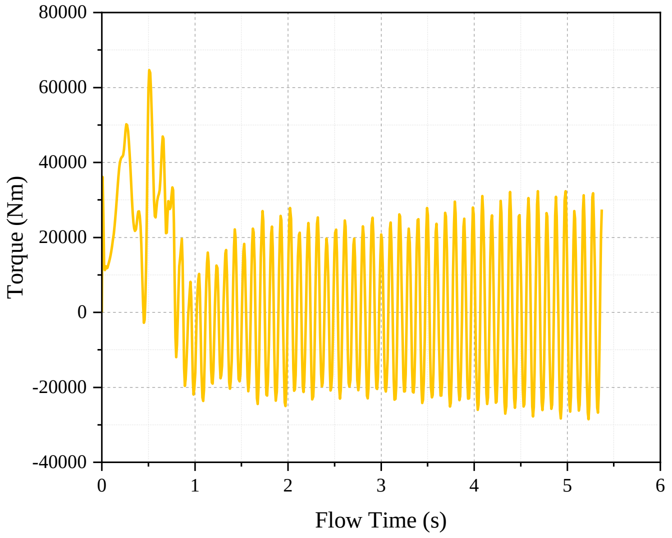

**Figure 20.** **Flow Time at a Flow Velocity of 4 m/s**

### *3-2-2- Azimuth Orientation vs. Flow Time*

Figure 21 presents the rotational orientation of the turbine rotor over time at a current velocity of 0.7 m/s, highlighting the rotor's dynamic behavior as it transitions from the start-up to steady-state operation. The horizontal axis represents flow time between 0 and 15 seconds, while the vertical axis denotes the rotor orientation angle, ranging from 0° to 360°, before resetting to 0° for the next rotation cycle. The graph shows an initial exponential rise in the orientation angle during the first rotation, corresponding to the acceleration period in which hydrodynamic forces gradually overcome the rotor's inertial resistance and frictional resistance. Following this start-up phase, the rotor attains a stable, nearly uniform rotational frequency, completing approximately seven full revolutions over the 15-second simulation. Periodic resetting to 360° confirms the cyclic nature of rotational motion applied in the numerical model. This consistent pattern indicates that, at a flow velocity of 0.7 m/s, the turbine develops sufficient torque to maintain self-sustained rotation, although at a relatively low angular velocity compared to higher flow speeds.

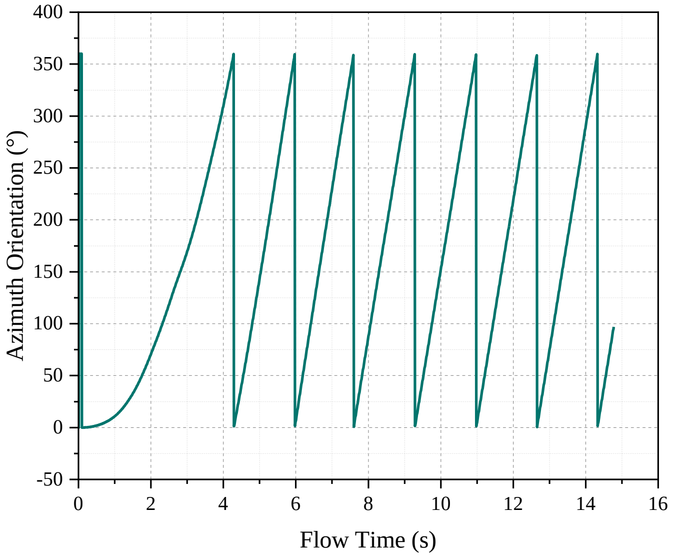

**Figure 21.** **Azimuth Orientation vs. Flow Time at 0.7 m/s**

Figure 22 illustrates the progression of rotor orientation over time at a current velocity of 2 m/s, demonstrating the turbine's dynamic rotational behavior as it shifts from an acceleration phase to a steady operating condition. The X-axis indicates flow time between 0 and 10 seconds, while the Y-axis denotes the rotor orientation angle, which increases continuously from 0° to 360° before repeating to 0°, representing a complete revolution. The plotted pattern indicates that the turbine completes approximately 15 full rotations in 10 seconds, indicating a substantially higher rotational speed than at 0.7 m/s. This increase directly correlates with the higher hydrodynamic energy available at greater flow velocities. During the first second, the curve exhibits a non-linear, exponential-like rise, reflecting the rapid increase in torque generated by the interaction between the incoming current and the blade surfaces, allowing the rotor to overcome inertial resistance faster than at lower-speeds. Beyond approximately one second, the curve response transitions to a consistent periodic waveform with uniform amplitude and frequency, indicating that the turbine has reached a steady-state condition in which aerodynamic torque, drag forces, and rotational inertia are balanced. This leads to sustained and stable rotation without significant fluctuations.

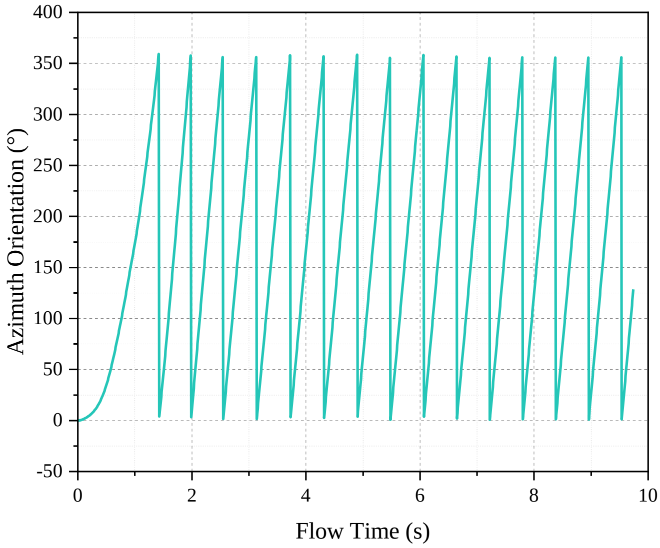

**Figure 22.** **Azimuth Orientation vs. Flow Time at 2 m/s**

Figure 23 presents the Orientation versus Flow Time graph for a turbine operating at a current speed of 3 m/s, highlighting the transition from the initial acceleration phase to steady rotational motion. The plotted curve exhibits a clear periodic pattern with consistently spaced peaks, indicating regular rotation cycles in which approximately 15 complete revolutions are achieved within 6.39 seconds. At the beginning of the simulation ($t \approx 0$), the orientation angle increases non-linearly, reflecting the acceleration phase during which the turbine blades rapidly gain rotational momentum due to enhanced hydrodynamic forces generated at this flow velocity. The sharp rise observed between 0 and approximately 1 second indicates a pronounced angular acceleration ($\alpha$) as the turbine overcomes inertial and hydrodynamic resistance. After this acceleration stage, the curve transitions smoothly to a more linear, periodic trend, indicating that the system has reached a steady-state operating regime with a relatively constant angular velocity. This response shows that, at a flow velocity of 3 m/s, the turbine receives sufficient kinetic energy to achieve rapid, stable, and uniform rotation, compared to lower flow speeds.

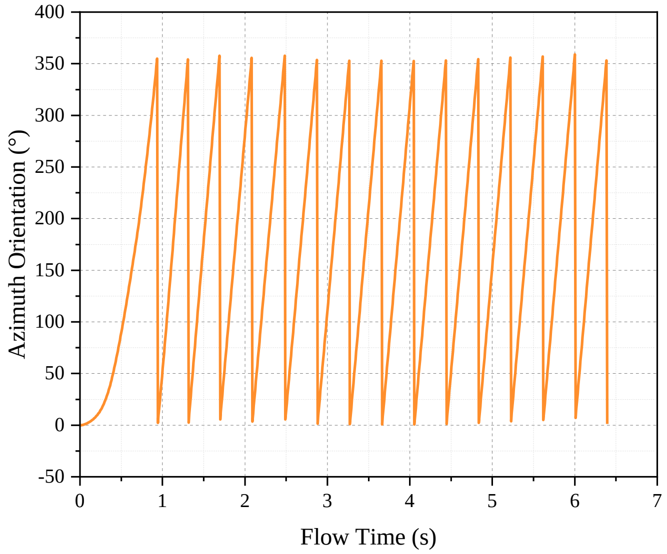

**Figure 23.** **Azimuth Orientation vs. Flow Time at 3 m/s**

Figure 24 illustrates the relationship between rotor orientation angle and flow time for the turbine operating at a current speed of 4 m/s, highlighting the transition from the initial acceleration phase to steady-state rotation. The graph shows two distinct phases in the turbine's rotational dynamics. During the initial acceleration phase (0–1 second), the rotor orientation increases non-linearly, indicating rapid angular acceleration as the aerodynamic torque generated by the fluid surpasses the combined resisting torques arising from inertia and friction. This sharp rise reflects the turbine blades' swift adaptation to the higher flow velocity and the corresponding increase in hydrodynamic forces. After approximately 1 second, the system transitions to a stable operation phase, where the orientation angle progresses in a regular, periodic manner, demonstrating that the turbine has reached a constant angular velocity. Compared to the 3 m/s case, the rotation cycles are denser, indicating a shorter rotation period and higher rotation frequency. This behavior confirms that at a flow speed of 4 m/s, the turbine achieves faster, more energetic rotation with higher torque and potential power output. However, it may also be subjected to stronger unsteady hydrodynamic forces on the blades.

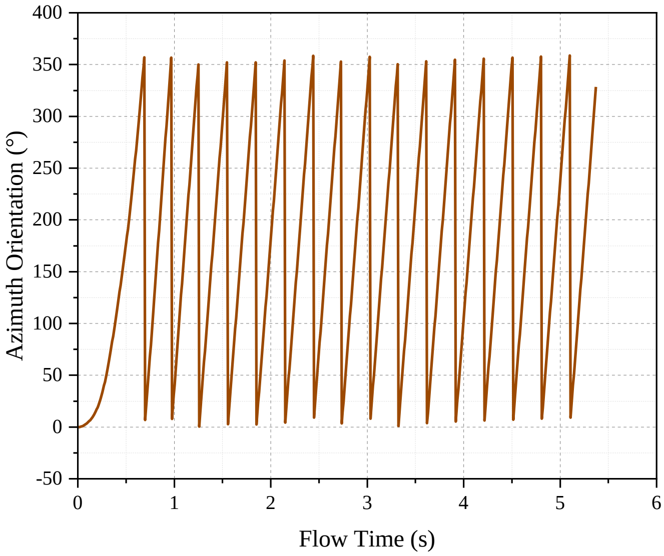

**Figure 24.** Azimuth Orientation vs. Flow Time at 4 m/s

### *3-2-3- Power and Efficiency*

From Table 3, it is clear that the turbine's angular velocity increases with rising flow velocity, moving from 3.3 rad/s at 0.7 m/s to 15.4 rad/s at 4 m/s. Higher flow velocities generate stronger hydrodynamic forces on the blades, resulting in faster rotation. The mechanical power output also increases significantly, from 1.274 kW at 0.7 m/s to 276.94 kW at 4 m/s, which follows the expected cubic relationship between power and flow velocity.

**Table 3.** Final Turbine Power Output and Final External Output Power

| No. | Current Velocity (m/s) | Angular Velocity (rad/s) | Turbine Power (kW) | Turbine Efficiency |
|---|---|---|---|---|
| 1 | 0.7 | 3.3 | 1.274 | 0.413 |
| 2 | 2 | 10.6 | 30.592 | 0.425 |
| 3 | 3 | 13.7 | 136.83 | 0.563 |
| 4 | 4 | 15.4 | 276.94 | 0.481 |

Turbine efficiency does not increase continuously across all velocities. The highest efficiency of 0.563 is reached at 3 m/s, indicating that this speed represents the optimal operating condition for the present turbine design. At 4 m/s, the efficiency decreases to 0.481, likely due to hydrodynamic factors, including stronger flow separation, partial blade stall, and turbulence-related losses at higher rotational speeds. In addition, the final electrical power output increases nonlinearly due to mechanical transmission losses of about 70% and electrical system losses of about 10%. These highlights emphasise the need to improve not only the turbine's hydrodynamic but also the overall energy conversion system to enhance total efficiency.

The comparison between the CFD torque-based power values and theoretical predictions shows that the efficiency results are consistent with both the Betz limit and the Blade Element Momentum Theory (BEMT). The efficiencies obtained in this study range from 0.413 to 0.563, remaining within the physically valid range and do not exceed the Betz limit of 0.593. At lower inflow velocities, the efficiency is slightly reduced because viscous effects and weaker blade interaction become more influential, consistent with theoretical expectations. At higher inflow velocities of 3-4 m/s, the turbine operates under more stable hydrodynamic conditions and reaches its maximum efficiency without exceeding theoretical performance limits.

The corresponding CFD-derived power outputs of 1.274 to 276.94 kW also follow the cubic relationship between velocity and power ($P \propto v^3$). This consistency further confirms that the CFD model captures the flow behavior predicted by classical turbine theory. Based on these comparisons, the CFD results are considered reliable, as they closely align with the Betz theoretical maximum efficiency and BEMT-based power trends, thereby validating the accuracy of the simulation setup and boundary conditions

## 4- Conclusion

This study presented a numerical investigation of the hydrokinetic performance and flow characteristics of a vertical-axis ocean current turbine using Computational Fluid Dynamics (CFD) through both steady-state and transient approaches. The simulation framework effectively provided an in-depth understanding of performance parameters, including torque output, power coefficient, and flow separation behavior, across multiple inflow velocities and rotational speeds. Steady-state simulations were used to obtain initial performance trends efficiently, enabling rapid evaluation of the influence of operating variables. Meanwhile, transient simulation captured dynamic, time-dependent flow patterns, vortex shedding mechanisms, and unsteady torque fluctuations that more closely represent real ocean flow conditions. The comparison confirmed that transient results provide higher predictive reliability for assessing turbine behavior in continuous, irregular ocean currents.

The findings indicate that the turbine demonstrates increasing efficiency with rising inflow velocity and rotational speed until reaching an optimal operational range, beyond which performance declines due to excessive turbulence, wake instability, and flow separation. The observed hydrokinetic responses underscore the importance of maintaining an appropriate tip-speed ratio, an optimized blade geometry, and effective rotational control strategies to maximize power extraction while minimizing negative flow effects. For future work, experimental validation is strongly recommended to strengthen numerical credibility, complemented by mesh sensitivity analyses, comparison of turbulence models, and simulations under multi-phase and marine-biofouling conditions. Additional research should address structural fatigue assessment, AI-based algorithm optimization, and techno-economic feasibility evaluation for real offshore deployment. Overall, this study provides a valuable reference for advancing the design and performance optimization of VAT-based ocean renewable energy systems.

## 5- Declarations

### *5-1- Author Contributions*

Conceptualization, R.A. and A.S.; methodology, R.A. and A.S.; software, R. and T.M.; validation, R.A. and A.D.N.; formal analysis, T.M.; investigation, A.S.; resources, R.; data curation, A.S.; writing—original draft preparation, A.S.; writing—review and editing, R.A. and T.M.; visualization, A.D.N.; supervision, R. and A.D.N.; project administration, A.D.N.; funding acquisition, T.M. and R. All authors have read and agreed to the published version of the manuscript.

### *5-2- Data Availability Statement*

The data presented in this study are available in the article.

### *5-3- Funding and Acknowledgments*

This research was conducted under a collaborative scheme between PT. PLN Research Institute and the Research Center for Hydrodynamics Technology (PRTH-BRIN). The authors gratefully acknowledge PT. PLN Research Institute for providing financial support for this study.

### *5-4- Institutional Review Board Statement*

Not applicable.

### *5-5- Informed Consent Statement*

Not applicable.

### *5-6- Conflicts of Interest*

The authors declare that there is no conflict of interest regarding the publication of this manuscript. In addition, the ethical issues, including plagiarism, informed consent, misconduct, data fabrication and/or falsification, double publication and/or submission, and redundancies have been completely observed by the authors.

## 6- References

[1] Finkl, C. W., & Charlier, R. (2009). Electrical power generation from ocean currents in the Straits of Florida: Some environmental considerations. Renewable and Sustainable Energy Reviews, 13(9), 2597–2604. doi:10.1016/j.rser.2009.03.005.

[2] Ponta, F. L., & Jacovkis, P. M. (2008). Marine-current power generation by diffuser-augmented floating hydro-turbines. Renewable Energy, 33(4), 665–673. doi:10.1016/j.renene.2007.04.008.

[3] Nunez, E. E., García González, D., López, O. D., Casas Rodríguez, J. P., & Laín, S. (2025). Fluid–Structure Interaction of a Darrieus-Type Hydrokinetic Turbine Modified with Winglets. Journal of Marine Science and Engineering, 13(3), 548. doi:10.3390/jmse13030548.

[4] Hantoro, R., Prananda, J., Mahmashani, A. W., Septyaningru, E., & Imanuddin, F. (2018). Performance investigation of an innovative Vertical Axis Hydrokinetic Turbine - Straight Blade Cascaded (VAHT-SBC) for low current speed. Journal of Physics: Conference Series, 1022(1), 12022. doi:10.1088/1742-6596/1022/1/012022.

[5] Velásquez, L., Rengifo, J., Saldarriaga, A., Rubio-Clemente, A., & Chica, E. (2025). Optimization of Vertical-Axis Hydrokinetic Turbines: Study of Various Geometric Configurations Using the Response Surface Methodology and Multi-Criteria Decision Matrices. Processes, 13(7), 1950. doi:10.3390/pr13071950.

[6] Inácio, R. G. da S., da Rosa, I. A., Avila, V. H., Rocha, L. A. O., Isoldi, L. A., Dias, G. da C., Gonçalves, R. A. A. C., & dos Santos, E. D. (2025). Numerical Investigation of Hybrid Darrieus/Savonius Vertical Axis Wind Turbine Subjected to Turbulent Airflows. Journal of Marine Science and Engineering, 13(10), 1979. doi:10.3390/jmse13101979.

[7] Ghafoorian, F., Hosseini Rad, S., & Moghimi, M. (2025). Enhancing Self-Starting Capability and Efficiency of Hybrid Darrieus–Savonius Vertical Axis Wind Turbines with a Dual-Shaft Configuration. Machines, 13(2), 87. doi:10.3390/machines13020087.

[8] Prasanna Vasan, V., VB, S. N., Alwin Thomson, A., Lakshmi Balaji, S., Dhatchna Moorthy, K., Subramania Pillai, S., ... & Nadaraja Pillai, S. (2025). Numerical simulation on the dynamic characteristics of VAWT with different cavity layouts. International Journal of Numerical Methods for Heat & Fluid Flow, 35(10), 3605-3635. doi:10.1108/HFF-10-2024-0803.

[9] Wong, K. H., Lee, K. Y., Ng, J. H., Wang, X. H., & Fazlizan, A. (2025). The effects of inertia on a straight-bladed vertical axis wind turbine. IOP Conference Series: Earth and Environmental Science, 1500(1), 12005. doi:10.1088/1755-1315/1500/1/012005.

[10] Shanab, B., & Untaroiu, A. (2025). Enhancing Dual-Rotor Vertical Axis Wind Turbines With Auxiliary Augmentation: Impact of Deflector Angle Orientation. Journal of Solar Energy Engineering , 147(6), 4069863. doi:10.1115/1.4069863.

[11] Kord, K., & Bazargan, M. (2024). Numerical Investigation on J-Shaped Straight-Bladed Darrieus Vertical Axis Wind Turbines Equipped with Gurney Flaps. International Journal of Energy Research, 8992210. doi:10.1155/2024/8992210.

[12] Prabowoputra, D. M., Prabowo, A. R., Yaningsih, I., Tjahjana, D. D. D. P., Laksono, F. B., Adiputra, R., & Suryanto, H. (2023). Effect of Blade Angle and Number on the Performance of Bánki Hydro-Turbines: Assessment using CFD and FDA Approaches. Evergreen, 10(1), 519–530. doi:10.5109/6782156.

[13] Stoessel, L., & Nilsson, H. (2015). Steady and unsteady numerical simulations of the flow in the Tokke Francis turbine model, at three operating conditions. Journal of Physics: Conference Series, 579(1), 12011. doi:10.1088/1742-6596/579/1/012011.

[14] Zimmer, G. (2008). Modelling and simulation of steam turbine processes: Individual models for individual tasks. Mathematical and Computer Modelling of Dynamical Systems, 14(6), 469–493. doi:10.1080/13873950802384001.

[15] Huang, W. D., Fan, H. G., & Chen, N. X. (2012). Transient simulation of hydropower station with consideration of three-dimensional unsteady flow in turbine. IOP Conference Series: Earth and Environmental Science, 15(5), 52003. doi:10.1088/1755-1315/15/5/052003.

[16] Rezaeiha, A., Montazeri, H., & Blocken, B. (2018). Towards accurate CFD simulations of vertical axis wind turbines at different tip speed ratios and solidities: Guidelines for azimuthal increment, domain size and convergence. Energy Conversion and Management, 156, 301–316. doi:10.1016/j.enconman.2017.11.026.

[17] Revuz, J., Hargreaves, D. M., & Owen, J. S. (2012). On the domain size for the steady-state CFD modelling of a tall building. Wind and Structures, 15(4), 313–329. doi:10.12989/was.2012.15.4.313.

[18] Ghasemian, M., Ashrafi, Z. N., & Sedaghat, A. (2017). A review on computational fluid dynamic simulation techniques for Darrieus vertical axis wind turbines. Energy Conversion and Management, 149, 87–100. doi:10.1016/j.enconman.2017.07.016.

[19] Stival, L. J. L., Brinkerhoff, J. R., Vedovotto, J. M., & de Andrade, F. O. (2022). Wake modeling and simulation of an experimental wind turbine using large eddy simulation coupled with immersed boundary method alongside a dynamic adaptive mesh refinement. Energy Conversion and Management, 268, 115938. doi:10.1016/j.enconman.2022.115938.

[20] Wang, L., Dong, M., Yang, J., Wang, L., Chen, S., Duić, N., Joo, Y. H., & Song, D. (2024). Wind turbine wakes modeling and applications: Past, present, and future. Ocean Engineering, 309, 118508. doi:10.1016/j.oceaneng.2024.118508.

[21] Lintermann, A. (2020). Computational meshing for CFD simulations. Clinical and Biomedical Engineering in the Human Nose: A Computational Fluid Dynamics Approach. Springer Singapore, Singapore. doi:10.1007/978-981-15-6716-2_6.

[22] diputra, R., Budisetyawan, D., Firdaus, N., Prabowo, A. R., Erwandi, & Rasgianti. (2024). Dynamic Characteristics of Trimaran Type Floating Ocean Current Power Plant. 2024 International Conference on Technology and Policy in Energy and Electric Power (ICTPEP), 140–144. doi:10.1109/ICT-PEP63827.2024.10733472.

[23] Fertahi, S. ed D., Belhadad, T., Kanna, A., Samaouali, A., Kadiri, I., & Benini, E. (2023). A Critical Review of CFD Modeling Approaches for Darrieus Turbines: Assessing Discrepancies in Power Coefficient Estimation and Wake Vortex Development. Fluids, 8(9), 242. doi:10.3390/fluids8090242.

[24] Huang, H., Sun, T., Zhang, G., Li, D., & Wei, H. (2019). Evaluation of a developed SST k-Ω turbulence model for the prediction of turbulent slot jet impingement heat transfer. International Journal of Heat and Mass Transfer, 139, 700–712. doi:10.1016/j.ijheatmasstransfer.2019.05.058.

[25] Mohamed, M. H., Ali, A. M., & Hafiz, A. A. (2015). CFD analysis for H-rotor Darrieus turbine as a low speed wind energy converter. Engineering Science and Technology, an International Journal, 18(1), 1–13. doi:10.1016/j.jestch.2014.08.002.

[26] Longest, P. W., & Vinchurkar, S. (2007). Effects of mesh style and grid convergence on particle deposition in bifurcating airway models with comparisons to experimental data. Medical Engineering & Physics, 29(3), 350–366. doi:10.1016/j.medengphy.2006.05.012.

[27] Paz, C., Suárez, E., Conde, M., & Vence, J. (2020). Development of a Computational Fluid Dynamics Model for Predicting Fouling Process Using Dynamic Mesh Model. Heat Transfer Engineering, 41(2), 199–207. doi:10.1080/01457632.2018.1522108.

[28] Zukas, J. A., & Scheffler, D. R. (2000). Practical aspects of numerical simulations of dynamic events: Effects of meshing. International Journal of Impact Engineering, 24(9), 925–945. doi:10.1016/S0734-743X(00)00012-9.

[29] Gobat, J. I., & Grosenbaugh, M. A. (2006). Time-domain numerical simulation of ocean cable structures. Ocean Engineering, 33(10), 1373–1400. doi:10.1016/j.oceaneng.2005.07.012.

[30] Welahettige, P., & Vaagsaether, K. (2018). Comparison of OpenFOAM and ANSYS Fluent. Proceedings of the 9th EUROSIM Congress on Modelling and Simulation, EUROSIM 2016, the 57th SIMS Conference on Simulation and Modelling SIMS 2016, 142, 1005–1012. doi:10.3384/ecp171421005.

[31] Xiao, Q., Liu, W., & Incecik, A. (2013). Flow control for VATT by fixed and oscillating flap. Renewable Energy, 51, 141–152. doi:10.1016/j.renene.2012.09.021.

[32] Arini, N. R., Turnock, S. R., & Tan, M. (2022). The Effect of Trailing Edge Profile Modifications to Fluid-Structure Interaction of a Vertical Axis Tidal Turbine Blade. International Journal of Renewable Energy Development, 11(3), 725–735. doi:10.14710/ijred.2022.44669.

[33] Ayachi Amar, A., Berkache, A., Amroune, S., Noura, B., & Boumehani, A. (2022). Numerical Modeling of Dynamic Stall in a Vertical Axis Wind Turbine. Academic Journal of Manufacturing Engineering, 20(4), 135–143.

[34] Fernández-Jiménez, A., Álvarez-Álvarez, E., López, M., Fouz, M., López, I., Gharib-Yosry, A., Claus, R., & Carballo, R. (2021). Power performance assessment of vertical-axis tidal turbines using an experimental test rig. Energies, 14(20), 6686. doi:10.3390/en14206686.